AGU PUBLICATIONS

Geochemistry, Geophysics, Geosystems

RESEARCH ARTICLE
10.1002/2016GC006752

Key Points:
- Successful characterization and identification of tsunami-induced deposits by rock-magnetism and mineralogy
- Different provenance of the sediment deposits related to two distinct tsunamigenic events PV1 and PV2
- Magnetic properties could reflect the effect of selective transport and deposition during each individual tsunami event

Supporting Information:
- Supporting Information S1

Correspondence to:
M. F. Bógalo,
mfbogalo@ubu.es

Citation:
Bógalo, M. F., M.-T. Ramírez-Herrera, A. Goguitchaichvili, D. Rey, K. J. Mohamed, M. Calvo-Rathert, and N. Corona (2017), Magnetic signature of the 22 June 1932 tsunami deposits (Jalisco, Mexican Pacific coast), *Geochem. Geophys. Geosyst.*, *18*, 2370–2387, doi:10.1002/2016GC006752.

Received 5 DEC 2016
Accepted 26 MAY 2017
Accepted article online 2 JUN 2017
Published online 26 JUN 2017

Magnetic signature of the 22 June 1932 tsunami deposits (Jalisco, Mexican Pacific coast)

M. F. Bógalo[1], M.-T. Ramírez-Herrera[2], A. Goguitchaichvili[3], D. Rey[4], K. J. Mohamed[4], M. Calvo-Rathert[1], and N. Corona[5]

[1]Departamento de Física, Escuela Politécnica Superior, Universidad de Burgos, Burgos, Spain, [2]Laboratorio Universitario de Geofísica Ambiental and Instituto de Geografía, Universidad Nacional Autónoma de México, Circuito de la Investigación, Ciudad Universitaria, Coyoacán, México, [3]Laboratorio Universitario de Geofísica Ambiental, Instituto de Geofísica, Universidad Nacional Autónoma de México, Unidad Michoacán, UNAM-Campus Morelia, México, [4]Departamento de Geociencias Marinas y Ordenación del Territorio, Universidad de Vigo, Vigo, Spain, [5]Centro de Estudios en Geografía Humana, El Colegio de Michoacán A.C., Michoacán, México

Abstract Recent studies have demonstrated that rock-magnetic analysis may provide additional information to distinguish and characterize extreme marine inundation events such as tsunamis. Rock-magnetic proxies reinforce and improve the environmental evidences supplied by other methods, adding some decisive clues for the interpretation of the origin and genesis of the sedimentary deposits. Here we report rock-magnetic, XRD, and SEM microscopy results obtained in the Palo Verde estuary (Colima Pacific coast, Mexico) in order to enhance the tools for identification and reconstruction of two tsunami-induced deposits. The sedimentary sequence includes two sand units, a tsunami deposit (PV1) associated with the 22 June 1932 tsunami and a deeper sandy layer (PV2) related to a possible paleotsunami that occurred around 1300 C.E. Both sandy units are topped by finer grained units. Magnetic properties exhibit a significant correlation with the stratigraphy. High susceptibility (χ) and high saturation isothermal remanence (SIRM) values typical of high concentrations of (titano)magnetite are a distinctive feature of the most recent sandy tsunamigenic unit PV1 and the overlaying soil. The lower sandy tsunamigenic unit PV2 shows significantly lower χ and SIRM values, indicating lower concentration of (titano)magnetite in this unit and the overlaying clayey-silt unit. The latter also shows a higher coercivity component associated with (titano)hematite. Magnetic grain-size differences are also observed between PV1 and PV2 suggesting differences in hydraulic conditions at the time of deposition. The bulk mineralogical composition and sediment texture of these units also support the hypothesis of different provenances for each tsunamigenic unit as inferred from magnetic properties.

1. Introduction

Tsunami deposits are generated as a consequence of onshore inundation and backwash flow of large water bodies and exhibit many distinct characteristics, ranging from variations in the mineral composition and distribution to particle size range [*Atwater and Moore*, 1992; *Dawson and Shi*, 2000; *Moore et al.*, 2006; *Morton et al.*, 2007; *Richmond et al.*, 2011; *Ramírez-Herrera et al.*, 2007, 2012; *Goto et al.*, 2015]. During the last decade, several multidisciplinary studies have been carried out to identify and characterize extreme inundation deposits [e.g., *Kortekaas and Dawson*, 2007; *Ramírez-Herrera et al.*, 2007, 2012; *Font et al.*, 2010, 2013; *Engel and Brückner*, 2011; *Wassmer and Gomez*, 2011; *Shanmugam*, 2012; *Cuven et al.*, 2013; *Goto et al.*, 2014, 2015]. Since 2010, magnetic parameters such as magnetic susceptibility and anisotropy of magnetic susceptibility (AMS) have proved highly resolving in tsunami deposit research [*Font et al.*, 2010; *Wassmer et al.*, 2010]. So far, several studies have applied these techniques in environments in which tsunami or paleotsunami deposits are present [*Ramírez-Herrera et al.*, 2012, 2014, 2016; *Cuven et al.*, 2013; *Font et al.*, 2013; *Goguitchaichvili et al.*, 2013; *Schneider et al.*, 2014; *Černý et al.*, 2016; *Kain et al.*, 2014, 2016; *Wassmer and Gomez*, 2011; *Wassmer et al.*, 2015].

On the other hand, some of these studies have also included more detailed magnetic measurements, strengthening the identification, and characterization of tsunamigenic deposits in stratigraphic records [*Font et al.*, 2010; *Goguitchaichvili et al.*, 2013; *Veerasingam et al.*, 2014; *Černý et al.*, 2016; *Ramírez-Herrera*

et al., 2016], and providing useful proxies that reinforce the information supplied by the tsunamigenic signature detected by more traditional methods (stratigraphical, geomorphological, sedimentological, geochemical, microfossil, palynological, mineralogical, and archaeological) [e.g., *Ramírez-Herrera et al*., 2007, 2012; *Shanmugam*, 2012; *Spiske et al*., 2013]. The basis for the use of magnetic properties as an environmental assessment tool is rooted on the principle that magnetic properties are sensitive to the mineralogy, concentration, and grain-size distribution of magnetic particles, which can be altered by geology, transport, sorting, and postdeposition processes.

The Pacific coast of Mexico (Figure 1a) is seismically active, and the subduction beneath the North American plate of both the Rivera and Cocos plates has produced large earthquakes and tsunamis in historical time. Typically, moment magnitude (Mw) 7.3–8.2 earthquakes occur about every 80 years [*Singh et al*., 1985], and larger Mw $>$ 8.5 have occurred less frequently (e.g., 28 March 1787 Mw 8.6 earthquake, off the Guerrero and Oaxaca coast) [*Suarez and Albini*, 2009]. On 3 June 1932, as a result of the rupture of the Rivera-North America plate interface, a surface-wave magnitude (Ms) 8.2 earthquake was recorded, the biggest one in the last century. Two aftershocks on 18 June (Ms 7.8) and 22 June (Ms 6.9) followed the main shock [*Singh et al*., 1981]. More recently, on October 1995, an Mw 8.0 earthquake hit the southern coast of Colima (Figure 1a). All of the above mentioned earthquakes produced tsunamis [*Cumming*, 1933; *Sánchez and Farreras*, 1993; *Corona and Ramírez-Herrera*, 2012]. However, the 22 June 1932 event (the second most destructive recorded in the Pacific coast of Mexico) caused an abnormally large one, considering its Ms 6.9 magnitude [*Okal and Borrero*, 2011; *Corona and Ramírez-Herrera*, 2012].

Several studies were already carried out in tsunamigenic deposits at Mexican Pacific coast, which proved the effectiveness of environmental magnetic techniques for improving the identification of the tsunami-induced deposits [*Goguitchaichvili et al*., 2013; *Černý et al*., 2016; *Ramírez-Herrera et al*., 2016]. The identification and characterization of the magnetic minerals in the tsunamigenic units helped to solve questions about the sediment provenance and the energy of the events. In general terms, different mineralogy as well as magnetic grain-size characterize these energetic events and distinguish from the background sediment. The aim of the present study is the magnetic characterization and identification of historical tsunami deposits, specifically those of the 22 June 1932 event and other prehistoric events in the Palo Verde (PV) estuary (Cuyutlán, Colima). The analysis of multiple proxies, including magnetic parameters, is especially useful in regions as the Pacific coast of Mexico, because the conservation of geologic information is affected by the inherent environmental characteristics of the tropics and frequent storms (hurricanes). *Ramírez-Herrera et al*. [2014] identified two probable tsunamis in the Palo Verde estuary analyzing different multiproxy data, including both magnetic susceptibility (χ) and AMS. We performed new detailed magnetic and mineralogical measurements and reevaluated these preliminary results, clearly improving the characterization of the sedimentary deposit bearing tsunamigenic units.

2. Geological Setting and Sample Materials

The Palo Verde estuary (PV), East of Cuyutlán, Colima, is located behind a sand-barrier overlain by a series of sand dunes $\sim$7.5 m above sea level (masl) near the PV site (Figures 1b and 1c). Inland, the Laguna Cuyutlán, a back-barrier lagoon, is fringed by mangrove swamps. The NW portion of Laguna Cuyutlán is characterized by saltpans (locally known as "Salinas"). The study site is located behind $\sim$7 m sand dunes and in a coastal plain occupied by mangrove marshes (Figure 1c). Intermediate to basic extrusive igneous rocks characterize the north of the studied area and granites are locally exposed [*Lancin and Carranza*, 1976]. Locally, the sands from the shore are rich in iron oxides [*Carranza-Edwards et al*., 2009] and the beach berm and intertidal beach zone show enrichment of heavy minerals [*Ramírez-Herrera et al*., 2014]. This is because the Cuyutlán lagoon barrier beach is constructed by sediments originating in the Armería River, whose mouth lies 7 km southeast of Palo Verde. Volcanic rock fragments are transported by the longshore currents, which have SE-NW directions [*Carranza-Edwards et al*., 2009]. The Colima volcano, the historically most active volcano from Mexico [*Sulpizio et al*., 2014] is located 80 km NE of Palo Verde site. This volcano belongs to the Quaternary Colima volcanic complex [*Verma and Luhr*, 1993]. Lower Cretaceous andesite outcrops corresponding to this volcanic activity are found just 3.5 km NE of the study area [*Servicio Geológico Mexicano*, 2000].

The PV estuary may be considered as well suited for tsunami deposit studies because it provides a vast amount of information which may be retrieved from a survey performed after the 1932 earthquake and

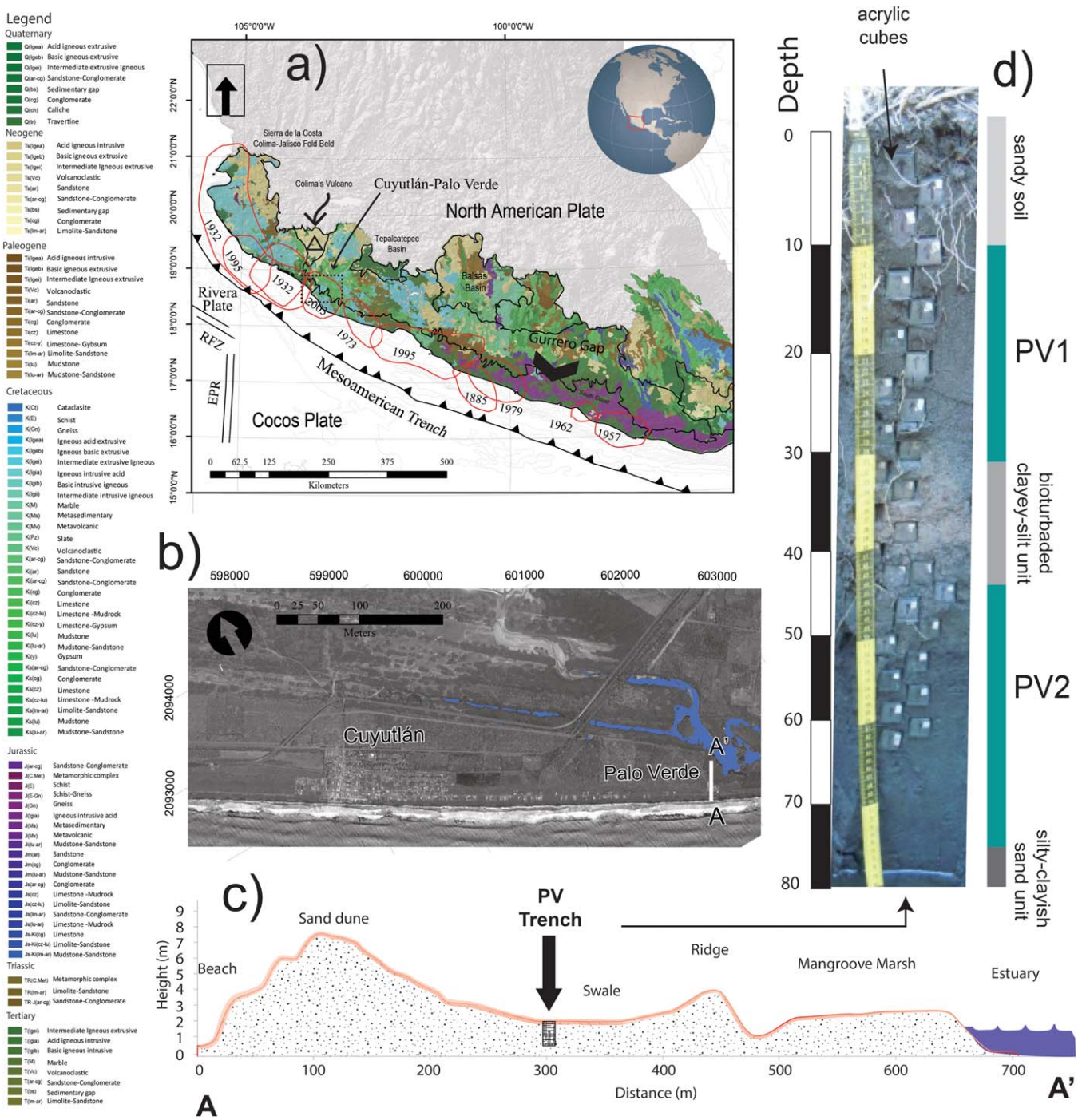

Figure 1. Seismotectonic and geologic setting. (a) Mexican subduction zone and seismic rupture areas—RFZ: Rivera fracture zone, EPR: East Pacific rise, circles in red color: rupture areas of most significant events in the last century. (b) Palo Verde estuary, white line shows trace of topographic profile shown in Figure 1c. (c) Topographic profile and location of trench PV. (d) Photo showing in situ collection of samples for magnetic properties studies.

tsunami [*Cumming*, 1933; *Corona and Ramírez-Herrera*, 2012, 2015] and from an investigation of the well-preserved geological signatures of past tsunamis that has identified the 1932 and a predecessor tsunami [*Ramírez-Herrera et al*., 2014]. In addition, *Corona and Ramírez-Herrera* [2012] and *Ramírez-Herrera et al*. [2014] reported tsunami-scour fans connected with the over-wash flow in Cuyutlán, broken dune features formed by tsunami erosion, and remnant pedestals located in the estuary a few hundred meters inland.

In the present study, samples for magnetic experiments were collected from a trench wall (PV) located approximately 270 m inland at an elevation of 2.0 masl (18.8987°N, 104.0338°W) (Figures 1b and 1c). Sampling was performed in situ in the trench using standard acrylic cubes for magnetic property analyses. Cubes were inserted in the wall from the surface to the bottom of the trench sequentially with no intervals in between, to recover a complete section of the stratigraphic units (Figure 1d) (for a detailed explanation of the technique see *Wassmer and Gomez* [2011], *Ramírez-Herrera et al*. [2012], and *Černý et al*. [2016]). The samples measured in this study are the same as those previously used for the AMS analysis by *Ramírez-Herrera et al*. [2014].

The Palo Verde profile can be divided into five distinct units (Figure 1d) [*Ramírez-Herrera et al*., 2014]. Two of them are sand beds associated with tsunamigenic events: PV1, at 10–32 cm depth and PV2, between 45.5 and 77 cm. Both units exhibit geological signatures typical of common tsunami deposits (normally graded sand beds, scattered pebbles near the base, erosional lower contact, increase in abundance marine-brackish diatoms, low organic content, and increase in elemental concentration of paleosalinity geochemical indicators) [*Ramírez-Herrera et al*., 2014]. The other units consist of an uppermost sandy soil (0–10 cm) and a bioturbated orange-brown clayey-silt unit (32–45.5 cm) interbedded between PV1 and PV2 that shows large differences in grain size, organic content, and geochemical composition [*Ramírez-Herrera et al*., 2014]. The lowest silty-clayish sand unit (77–91.5 cm) was not completely sampled because it is located below the water table. *Ramírez-Herrera et al*. [2014] suggested that the sand unit PV1 was linked to the 22 June 1932 tsunami and that PV2 is related to a possible older event that happened around 1300 C.E. (1284–1389 C.E.).

3. Methods

Samples were collected as explained above from an 80 cm deep trench by using 8 cm^3 plastic boxes and 35 samples were obtained. Low-field magnetic susceptibility (χ) expressed in mass-unit (m^3/kg) was measured with a Kappabridge KLY4 (AGICO Ltd., applying a 300 A/m field). A dual frequency (470 and 4700 Hz) Bartington MS2 susceptometer was utilized to evaluate the contribution of fine-grained ferrimagnetic particles near the SP/SD threshold based on the frequency-dependent susceptibility parameter ($\chi_{fd}\% = 100 \times (\chi_{fd}/\chi_{lf})$, where $\chi_{fd} = \chi_{lf} - \chi_{hf}$, χ_{lf} and χ_{hf} being magnetic susceptibilities at low and high frequency, respectively) [e.g., *Maher*, 1986; *Dearing et al*., 1996]. Anhysteretic remanent magnetization (ARM) was given to the samples by demagnetizing them in a peak alternating field (AF) of 100 mT in the presence of a 0.05 mT direct current (DC) bias field using the 2G cryogenic magnetometer in-line system (2G-enterprise). The ARM susceptibility (χ_{ARM}) was obtained by dividing the mass-normalized ARM by the DC bias field. A variable field translation balance (MMVFTB) was used to perform the following series of experiments: isothermal remanent magnetization (M_r or IRM) acquisition curves (1 T peak field), hysteresis loops ($\pm$1 T), backfield curves in order to measure coercivity of remanence, and magnetization versus temperature ($M_s - T$) thermomagnetic curves in a 38 mT DC field. The latter experiment was performed in air, heating up to 700°C and cooling down to room temperature with a 30°C/min rate. Hysteresis loops after subtraction of paramagnetic and diamagnetic contributions allowed determination of hysteresis parameters like saturation magnetization (M_s), saturation remanent magnetization (M_{rs} or SIRM), and coercive field (B_c). S_{-200} ratio was determined as (1–IRM_{-200mT}/SIRM)/2 [*Bloemendal et al*., 1992]. The RockMagAnalyzer 1.1 software [*Leonhardt*, 2006] was used to visualize and interpret these parameters.

Thirteen samples were selected to perform detailed stepwise IRM acquisition curves up to 2 T using a M2T-1 pulse magnetizer and were consolidated with nonmagnetic plaster for these experiments. Twenty-five to twenty-seven field steps from 17 to 2000 mT were used to analyze the IRM curves and evaluate the magnetic coercivity components [*Kruiver et al*., 2001; *Heslop et al*., 2002]. IRM acquisition curves were approximated by a number of log-Gaussian (CLG) curves, using the IRM-CLG Excel spreadsheet developed by *Kruiver et al*. [2001]. Each curve is characterized by its SIRM intensity (IRM at 2 T), mean coercivity ($B_{1/2}$), and dispersion parameter (DP) [*Robertson and France*, 1994]. Thereafter, a composite IRM with 2, 0.4, and 0.12 T fields applied in orthogonal directions was imparted to the samples and subsequently thermally demagnetized in 17 temperature steps from room temperature up to 680°C, following *Lowrie* [1990].

Several representative samples of the trench (at least two per unit) were selected at depths where relevant changes were observed in geochemical and magnetic properties as well as sedimentological features. The

presence of minerals associated with these features was analyzed through Field Emission Scanning Electron Microscopy (FE-SEM) at the University of Vigo using a JEOL JSM-6700F microscope. The observations were performed on carbon-coated epoxy resin embedded polished samples using the FE-SEM operating in back scattering mode (BS). The energy dispersive X-ray spectroscopy probe from the electron microscope was used to analyze relevant minerals and determine their chemical composition semi quantitatively by means of an EDS Oxford Inca Energy 300 SEM.

XRD determinations and semiquantitative analyses were performed with a SIEMENS D-5000 diffractometer at the University of Vigo on representative samples from the modern beach (inter and supratidal areas), and from the trench (topsoil, PV1, clayey-silt unit, and PV2).

4. Results

4.1. Magnetic Mineralogical Results

Magnetic susceptibility (χ), saturation remanence (M_{rs} or SIRM at 1 T), and saturation magnetization (M_s) are indicators of magnetic concentration. Observed curve shapes are similar for these studied parameters, with the exception of M_s in the soil and the uppermost 20 cm of PV1 (Figure 2), indicating that the magnetic signal is mainly influenced by the concentration of ferromagnetic minerals (in a broad sense). The values of these parameters are relatively high and homogeneous for most PV1. χ decreases sharply at the base of PV1 and downward into the clayey-silt unit, where a local minimum is reached at the maximum silt horizon. Then χ steadily increases downward along all the PV2 unit. The sharp decrease of the values of magnetic properties at the bottom of PV1 coincides with the sharp basal contact between the tsunami-induced deposit and the underlying clayey-silt layer.

Figure 3a shows a good correlation between χ and SIRM values ($r^2 = 0.9813$) confirming that ferromagnetic minerals control the magnetic susceptibility. Two clusters associated with the upper (uppermost soil and PV1) and the lower (clayey-silt unit and PV2) parts of the profile can be distinguished in the figure. The lowermost sample from PV1, located at 31 cm falls into the PV2 cluster and follows the tendency showed by the samples belonging to the clayey-silt unit. The anhysteretic remanent magnetization (ARM) is sensitive to the concentration of single domain (SD) ferrimagnetic particles (~0.03–0.06 μm) [e.g., *King et al.*, 1982; *Liu et al.*, 2012]. The ARM profile (Figure 2) displays quite a different behavior than the parameters described above, both in the uppermost and in the lowest part of the profile. Therefore, the observed differences from the other intensity-related magnetic parameters may be due to variations in the concentration of fine SD ferrimagnetic grains. On the other hand, the concentration of ferrimagnetic grains depends on the

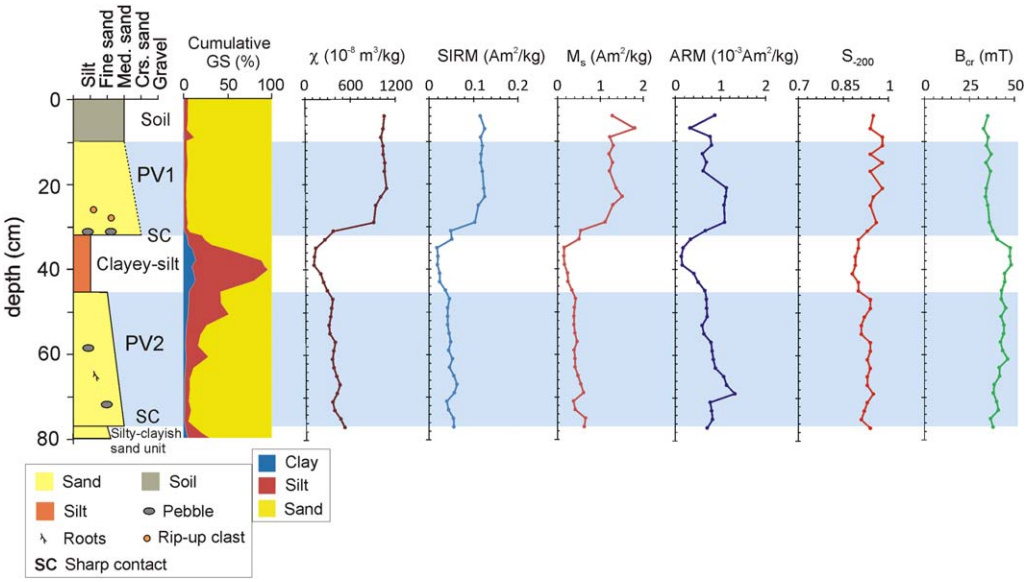

Figure 2. Palo Verde trench stratigraphy, cumulative grain size [*Ramírez-Herrera et al.*, 2014] and selected rock-magnetic parameters related to magnetic mineralogy.

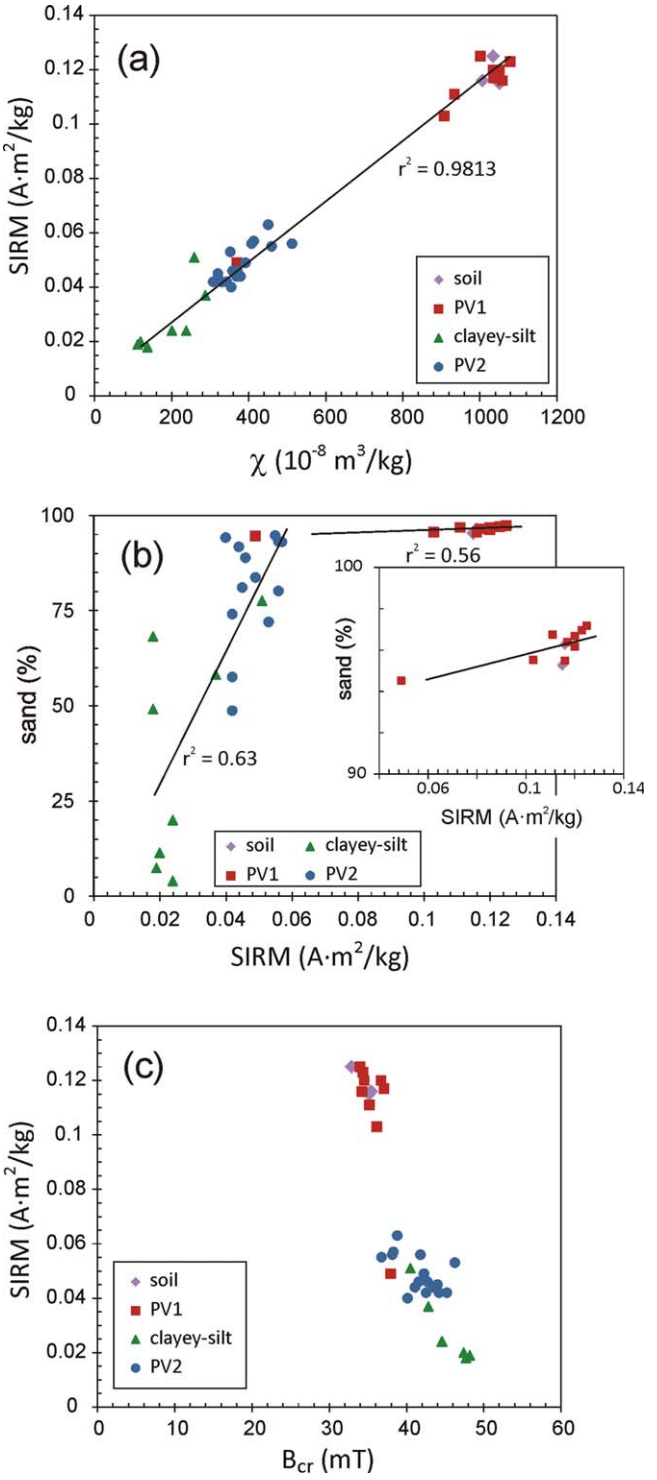

Figure 3. Biplots of (a) saturation remanent magnetization (SIRM) versus susceptibility (χ). (b) Sand percentage versus SIRM. (c) SIRM versus the coercivity of remanence (Bcr). The samples are well grouped according to their stratigraphy.

texture since SIRM and χ shows linear correlation with the sand percentage (Figures 2 and 3b). However, two trends with different slopes corresponding to the upper (soil and PV1) and the lower (clayey-silt and PV2) part of the profile can be observed (correlation parameter r^2 of 0.56 and 0.623, respectively) (Figure 3b).

The relative concentration of ferrimagnetic and antiferromagnetic minerals can be inferred from the S_{-200} ratio. Their values are close to 1 indicating that low coercive magnetic minerals dominate the magnetic remanence (Figure 2). However, slight differences are observed depending on the facies. Clayey-silt show the lowest values, indicating that the contribution of high coercive magnetic mineral is slightly higher in this unit than in PV1 and PV2. In the bivariate M_{rs} (SIRM) versus B_{cr} plot (Figure 3c), it is possible to clearly observe two clusters corresponding to the different units: soil-PV1 and PV2. Samples from the "PV2 cluster" contain less concentration of ferrimagnetic minerals but display higher coercivities compared to those from the "PV1 cluster." Samples from the clayey-silt unit show the most extreme behavior, with the lowest concentration of ferrimagnetic minerals and the highest coercivities. This slightly higher coercivity in the clayey-silt unit than in the tsunamigenic units could be both an effect of the magnetic grain size of the ferrimagnetic minerals (SD grains displaying a higher coercivity than MD grains) and the higher contribution of high coercivity minerals.

4.2. Magnetic Domain-State

Magnetic domain-state distribution along the profile can be inferred using frequency-dependent susceptibility (absolute χ_{fd} and percentage χ_{fd}%) and other combined ratios such as M_{rs}/χ, χ_{ARM}/χ, ARM/M_{rs} or the hysteresis ratios M_{rs}/M_s and B_{cr}/B_c (Figure 4). Frequency-dependent susceptibility is commonly used to determine the concentration of superparamagnetic (SP) ferrimagnetic grains near the superparamagnetic/stable single domain (SP/SD) boundary [e.g., *Forster et al.*, 1994; *Dearing et al.*, 1996]. χ_{fd}% values are very low in the entire profile, varying between 3.25% in the soil layer and 0.6% in the clayey-silt unit. Although the relative

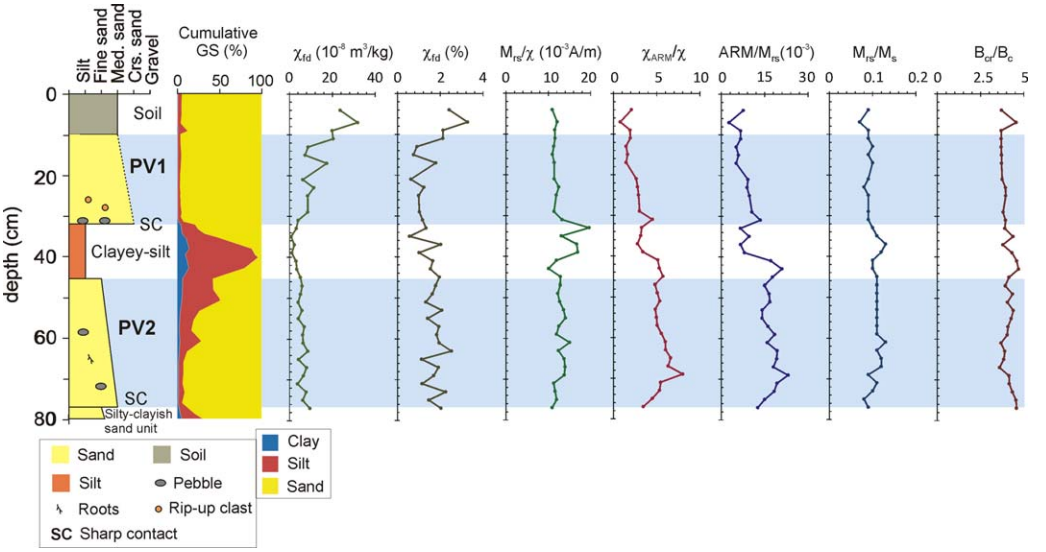

Figure 4. Rock-magnetic parameters which can be related to magnetic grain size versus depth.

contribution of these fine grains is not significant, the absolute values of χ_{fd} in the uppermost part of the profile (20–31 $\times$ 10^{-8} m^3/kg) are high and comparable to those obtained in previous environmental studies [e.g., *Maher*, 1998; *Torrent et al*., 2007; *Bógalo et al*., 2014; *Lyons et al*., 2014] in which the pedogenic magnetic grain contribution was important.

Small particles of magnetite yield higher M_{rs}/χ, χ_{ARM}/χ, and ARM/M_{rs} ratio values, whereas low values are related to coarser grain sizes [e.g., *Evans and Heller*, 2003; *Peters and Dekkers*, 2003; *Liu et al*., 2012]. Susceptibility (χ) is a parameter not only affected by ferromagnetic minerals (in a broad sense) but also affected by diamagnetic, paramagnetic, and SP grains. The most powerful parameter detecting the relative abundance of fine SD magnetic grains is ARM/M_{rs}, since remanences exclude these paramagnetic/diamagnetic and SP contributions. χ_{ARM}/χ and ARM/M_{rs} profiles show similar behavior with depth. The values of these parameters increase with depth in the tsunamigenic units PV1 and PV2 until 69 cm. The lowest values observed in PV1 suggest that the relative amount of coarser ferrimagnetic minerals is higher in this unit than in PV2. A significant shift is observed in the intermediate clayey-silt unit, which could be associated not only with ferrimagnetic grain-size variations but also with a minor contribution of high coercivity minerals. The ratio M_{rs}/χ is quite uniform in PV1, showing values slightly lower than in PV2 and corroborating the magnetic grain-size differences between PV1 and PV2 units observed with the previous parameters. The values of the M_{rs}/M_s and B_{cr}/B_c ratios are rather constant in the whole profile, although in PV1 they are slightly lower than in PV2. The relationship between these two ratios is shown in a Day plot, together with theoretical mixing curves for magnetite [*Day et al*., 1977; *Dunlop*, 2002] (Figure 5). The experimental values fall into the pseudo-single-domain (PSD) area and samples from units PV1 and PV2 can be clearly distinguished. The values of the PV1 unit are well grouped, displaying a more homogeneous behavior, whereas those of PV2 are more scattered following the SD + MD trend and above

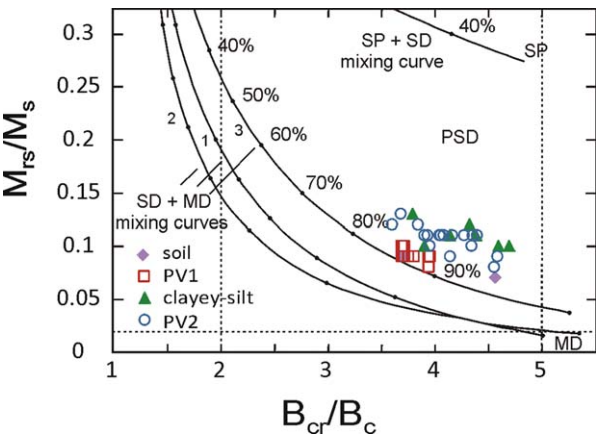

Figure 5. Hysteresis ratios (M_{rs}/M_s versus B_{cr}/B_c) plotted on a Day plot [*Day et al*., 1977] in linear scale for all the studied samples according to the legend. Theoretical mixing curves SD + MD and SD + SP for magnetite [*Dunlop*, 2002] are showed in the plot. PV1 and PV2 refer to the tsunamigenic sand units.

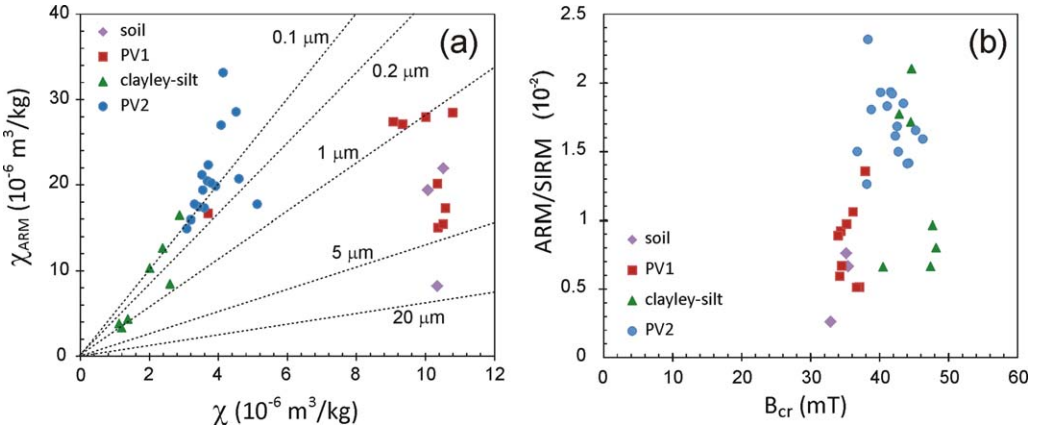

Figure 6. (a) Relationship between ARM susceptibility (χ_{ARM}) and low-field susceptibility (c) in the so-called King plot. The dashed lines correspond to the relationship between χ_{ARM} and χ for magnetite of different grain sizes (given in microns) [*King et al*., 1982]. T(b) Biplot of ARM/SIRM versus the coercivity of remanence (Bcr). Samples from the different tsunamigenic units PV1 and PV2 display different trends.

PV1 data. Deviations from the theoretical SD + MD trend could be due to several reasons including minor contributions of high coercivity minerals or variations in the Ti-content of titanomagnetite grains [*Dunlop*, 2002; *Özdemir and Dunlop*, 2014].

The bivariate χ_{ARM} versus χ plot or King plot [*King et al*., 1982] (Figure 6a) shows clear differences in grain size. In this diagram, changes in slope are related to grain-size variations, smaller grains yielding steeper slopes. Changes along a line of constant slope are indicative of magnetite concentration variations. Samples from the clayey-silt unit and those from the upper part of PV2 (up to 65 cm) follow a very good linear correlation ($r^2 = 0.92$), indicating a rather homogeneous grain-size distribution in that part of the profile. This behavior differs greatly from the one showed in the upper layers (soil and PV1) and in the bottom of the profile. In this case, nonlinear correlation data are probably due both to changes in concentration of magnetite and in grain size. In addition, soil and PV1 samples are close to the coarser magnetite PSD-MD grain-size area whereas those from the lower units (clayey-silt and PV2) are within the SD-PSD region. These grain-size differences can also be observed in Figure 6b. Two clusters (soil-PV1 units and the lower part of clayey-silt and PV2 unit) could also indicate that the mineralogy of the upper part of the profile mainly consists of coarser (titano)magnetite grains with lower coercivity whereas in the lower part finer grains of (titano)magnetite are associated with higher coercivities. Samples from the upper part of the clayey-silt unit with the highest coercivity values are not grouped in any cluster.

4.3. Magnetic Mineral Identification

IRM acquisition data modeling was performed in thirteen selected samples (supporting information Table S1 and Figure 7). Two distinctive magnetic components were identified by decomposition of the IRM acquisition curves using a cumulative log-Gaussian (CLG) function [*Kruiver et al*., 2001; *Heslop et al*., 2002; *Robertson and France*, 1994]: (1) a first component M is characterized by its low coercivity. It dominates the magnetic response, although the contribution percentage and mean coercivity field ($B_{1/2}$) values are different in each unit. The coercivity of this component is lower and very homogeneous in PV1 ($B_{1/2}$: ~43.7–43.9 mT) except for the lower sample ($B_{1/2}$: ~47.9 mT), intermediate in PV2 ($B_{1/2}$: ~47.9–51.3 mT) and higher in the clayey-silt unit ($B_{1/2}$: ~50.1–55 mT) (see supporting information Table S1).This component could be identified as detrital (titano)magnetite of different grain size and/or Ti-content; (2) a second component H of higher coercivity has been identified in the lowest sample of PV1, just at the boundary between PV1 and the clayey-silt unit, and in the clayey-silt and PV2 units. We want to stress the fact that in PV1 this component can only be found in the lowermost sample. The concentration of this second component varies between 2.6 and 5.9%, being highest in the clayey-silt unit. Its mean coercivity ($B_{1/2}$) lies between 371.5 and 446.7 mT in the clayey-silt unit and between 346.7 and 398.1 mT in PV2. This component could be related to fine-grained Ti-hematite.

The results of the thermal demagnetization of three-axial IRMs are showed in Figure 8. Slight differences can be observed among the soft component (0.12 T) curves, showing in all samples a wide unblocking

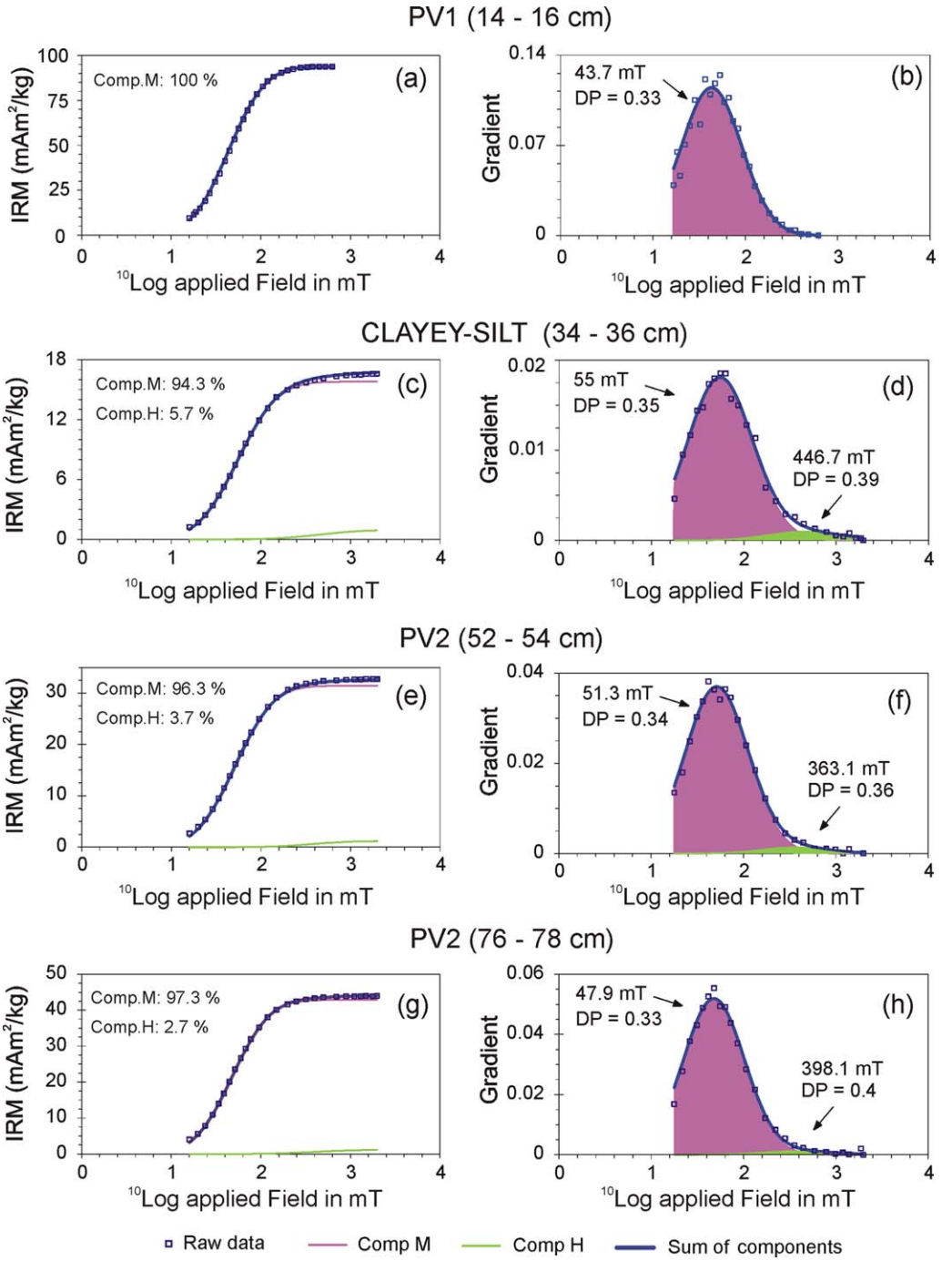

Figure 7. IRM unmixing analyses [*Kruiver et al.*, 2001; *Heslop et al.*, 2002] for four representative samples from the labeled stratigraphic units.

temperatures spectrum with maxima between 550 and 580°C, typical of magnetite or titanomagnetite with different Ti-content. In addition, a variable fraction of high coercivity minerals with maximum unblocking temperature higher than 650°C (2 T component), probably due to a small fraction of hematite, can be observed in the inset plots. This component appears in all measured samples, even in samples from the soil and PV1 in which it has not been possible to identify it by statistical decomposition of IRM, probably due to its very low concentration. The contribution of this high coercivity component is more evident in the clayey-silt unit.

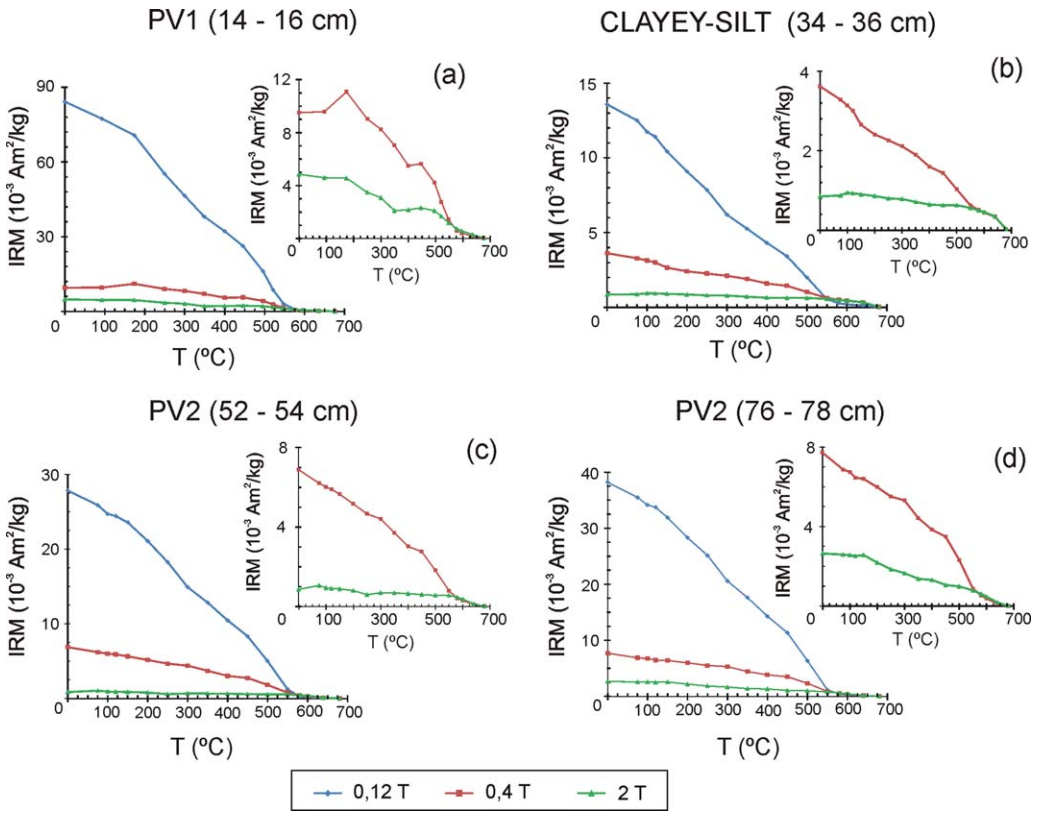

Figure 8. Representative examples of thermal demagnetization of three-axial isothermal remanent magnetization (IRM) experiments.

A detailed Curie temperature (T_c) analysis has been carried out along the whole profile (Figure 9). Figure 9a displays Curie point values for every stratigraphic position calculated with the two-tangent method proposed by *Grommé et al*. [1969]. Two types of thermomagnetic behavior can be observed in the heating curves: (1) curves of samples from the clayey-silt intermediate unit with two different phases corresponding to (Ti)magnetite (569–577°C) and a high-temperature phase, probably titanohematite (667–672°C); (2) the remaining curves exhibit a single phase and Curie temperatures typical of magnetite (or titanomagnetite). In this last case, the Curie temperature for samples from PV1 (between 570 and 579°C) is around 30°C higher than for those from PV2 (between 548 and 556°C), probably due to different Ti-content. Low-Ti-titanomagnetite/magnetite is identified as the low Curie temperature phase. The difference in Ti-content identified in the tsunamigenic units PV1 and PV2 could be related to a different origin of the magnetic grains. Samples from the clayey-silt units and those situated just above and just below have more variable values (546–577°C). In the cooling curves, T_c values of the low-temperature phase are very similar throughout the profile, mainly in the PV1 and PV2 units. In addition, the differences between the Curie temperature values from the heating and cooling curves (ΔT_c) for the (Ti)magnetite phase are dissimilar in PV1 and PV2 (supporting information Figure S1). ΔT_c is ~30–38°C for PV1 and ~7–15°C for PV2 (with exceptions at 47 and 69 cm). A possible explanation of this behavior could be that changes in Curie temperature could arise from cation reordering during heating in thermomagnetic experiments [*Bowles et al*., 2013].

4.4. Scanning Electron Microscopy (SEM) and XRD Analyses

In general terms, the results show that top soil, PV1 and PV2 consist of lithoarenites formed by intermediate to basic volcanic rocks including K feldspar and plagioclase, and abundant ferromagnesian minerals, likely olivine and pyroxenes (Figure 10). The grains are quite angular, poorly rounded and lack of typical subaqueous and high-energy surficial marks, particularly quartz grains (Figure 11). The composition and texture of the framework grains are very similar to the present-day beach. Matrix is thought to be mostly primary. It is thought that primary matrix in PV1 and PV2 has inhibited the intense alteration of lithic framework grains

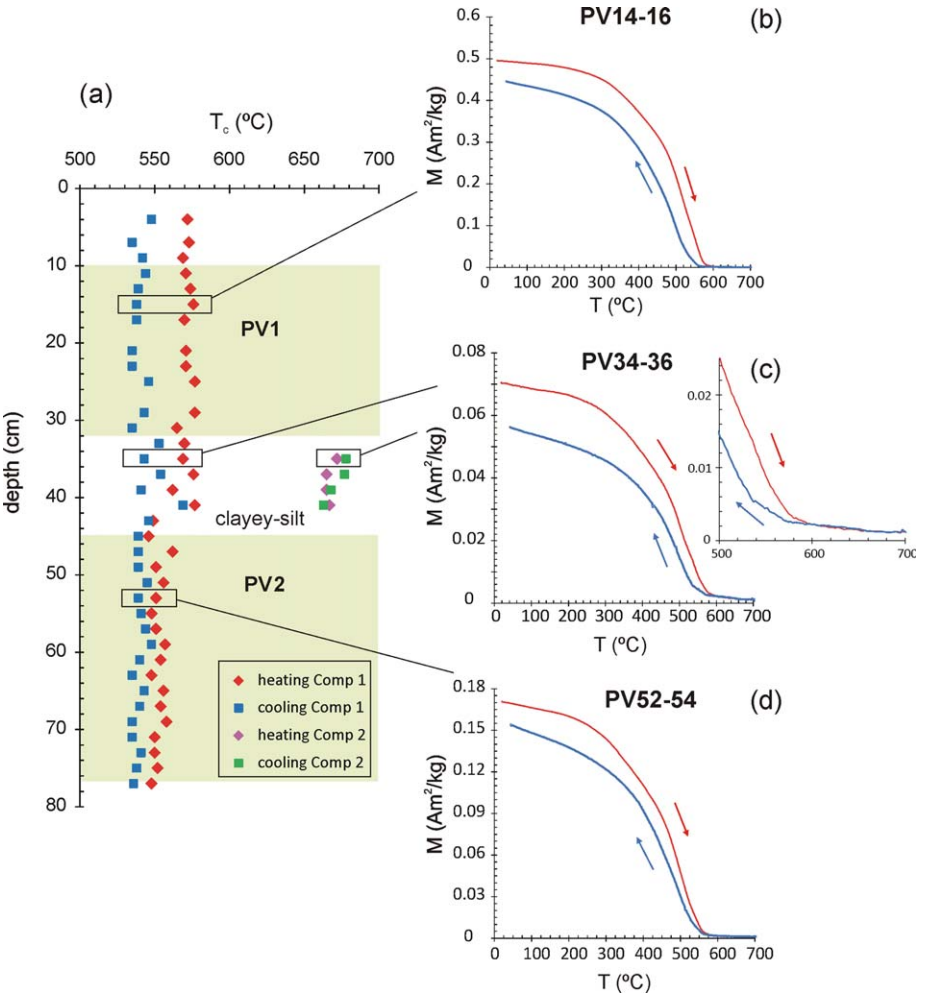

Figure 9. (a) Curie temperatures (T_c) calculated from the heating and cooling thermomagnetic curves. (b–d) Thermomagnetic curves for three representative samples. Low-temperature and high-temperature components (comp. 1 and comp. 2) are associated with (Ti)magnetite and (Ti)hematite, respectively.

observed in the clayey-silt unit, which is incipient in the topsoil. The occurrence of montmorillonite in the clayey-silt unit is interpreted as the result of the alteration of the friable volcanic glass and lithoclasts, and some feldspar. Fe-rich minerals are recognized by their brighter contrast. They occur both as discrete grains and forming part of lithic volcanic clasts (Figure 11). Iron, and iron-titanium oxides are frequent in a wide range on grain sizes, very often as small inclusions in lithic grains that preserve their original igneous texture. In general terms, surficial textures on silicates lack the sorting and textural characteristics observed in the beach sediments. It is thought that either they have not been exposed sufficiently to wave action that their original beach characteristics have been lost by reworking, or a combination of both. Some indication of chemical leaching is observed, although the sparsity of quartz grains makes difficult to assess the statistical significance of these observations (Figure 11).

Mineralogical composition between PV1 and PV2 is nearly indistinguishable and very similar to present-day intertidal beach sand and topsoil. The proportion of quartz and composition of the topsoil and PV1 framework grains is virtually identical (Figure 10). Major differences reside in the occurrence and preservation of a fine-grained clayey matrix in the topsoil. The composition of PV2 is slightly different, particularly in the iron oxides. In particular the leucoxene-type textures typical of titanomagnetites and/or ilmenohematite are more abundant, suggesting a different source. Both magnetic iron oxide grains and magnetic mineral inclusions in rock fragments are less abundant in this unit. Elemental mapping showed a fairly uneven distribution of Fe in the three studied units (Figure 10).

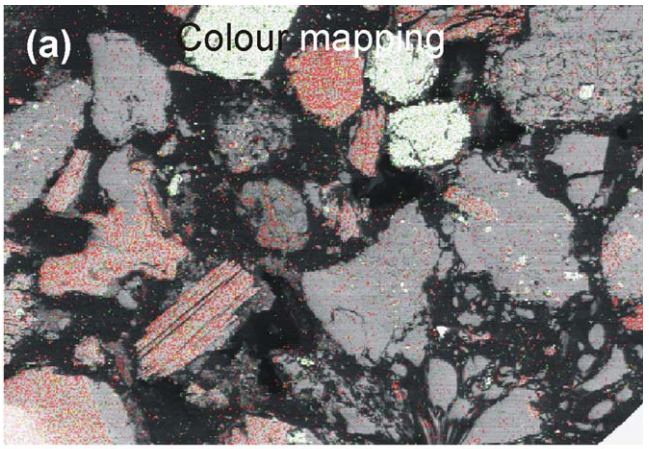

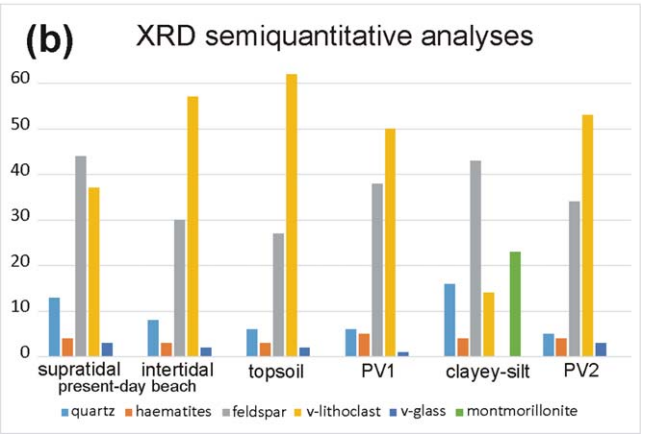

Figure 10. (a) EDX color mapping image of a polish-section from PV1. Red is Mg and green is Fe. (b) Summary of X-ray diffraction semiquantitative analyses.

No evidence of significant diagenesis that may have explained the observed differences in the magnetic properties between PV1 and PV2 was found, which is consistent with the absence of early diagenesis promotion such as high organic matter content (i.e., low Fe/χ_{lf} ratio of *Reitz et al*. [2004] and *Hofmann et al*. [2005]).

5. Discussion

5.1. Characterization of Tsunamigenic Units

Magnetic parameters correlate with the sedimentary stratigraphy (Figures 2 and 4), although this behavior is most evident in those parameters connected with type and concentration of ferrimagnetic minerals. There are two most relevant characteristics observed from the magnetic profiles: (1) the difference between the upper part (0–30 cm; soil and PV1 unit) and the units beneath (30–78 cm; clayey-silt and PV2 units); (2) the sharp change of the magnetic properties just in the contact between PV1 and the lower clayey-silt unit.

Regarding the former first distinctive characteristic, χ, SIRM, M_s, and ARM values in the soil and PV1 unit are more than 20 times higher than those obtained in other sedimentary deposits at the Mexican Pacific coast that include tsunamigenic units [*Černý et al*., 2016; *Ramírez-Herrera et al*., 2016]. This higher concentration of magnetic minerals in the Palo Verde site is attributed to contribution of local volcanic material. In fact, *Carranza-Edwards et al*. [2009] showed that beach sands in this area display enhanced iron oxide content. The good correlation between χ and SIRM (Figures 2 and 3a) and the magnetic mineral identification experiments (Figures 7–9) indicate that these rock-magnetic parameters are mainly controlled by the contribution of ferrimagnetic minerals (magnetite and Ti-magnetite) in the whole profile. Small differences between χ and SIRM could be associated with variations in the magnetic grain-size distribution (Figures 4 and 6) and/or minor high coercivity mineral contributions (Ti-hematite) (Figures 7–9).

The results obtained modeling IRM acquisition data have showed that the characteristics (SIRM, $B_{1/2}$, and DP) of the dominant low coercivity component identified as detrital (Ti)magnetite (component M) in PV1 are different from those obtained in other layers beneath. The most distinctive characteristic is its high concentration, as is showed by SIRM. The different values in both remanent coercivity (B_{cr}) and mean destructive field ($B_{1/2}$) of this component could be related not only to its diversity in grain size (Figures 4 and 6) but also to the Ti-content (and maybe the oxidation state). Differences in grain-size distribution between both PV1 and PV2 units have been detected. Coarser (Ti)magnetite grain contribution is more important in PV1 than in PV2. The values of ARM/SIRM in PV1 are indicators of MD + PSD grains, whereas coarser SD dominates PV2 [*Dearing et al*., 1997; *Peters and Dekkers*, 2003]. Pedogenic fine-grained magnetite has mainly been detected in the upper part of the profile (soil and the uppermost PV1). From SEM experiments a secondary montmorillonite-rich matrix as the result of alteration of volcanic grains and fine-grained Fe-rich mineral could be detected in the clayey-silt unit. However, frequency-dependent susceptibility parameters

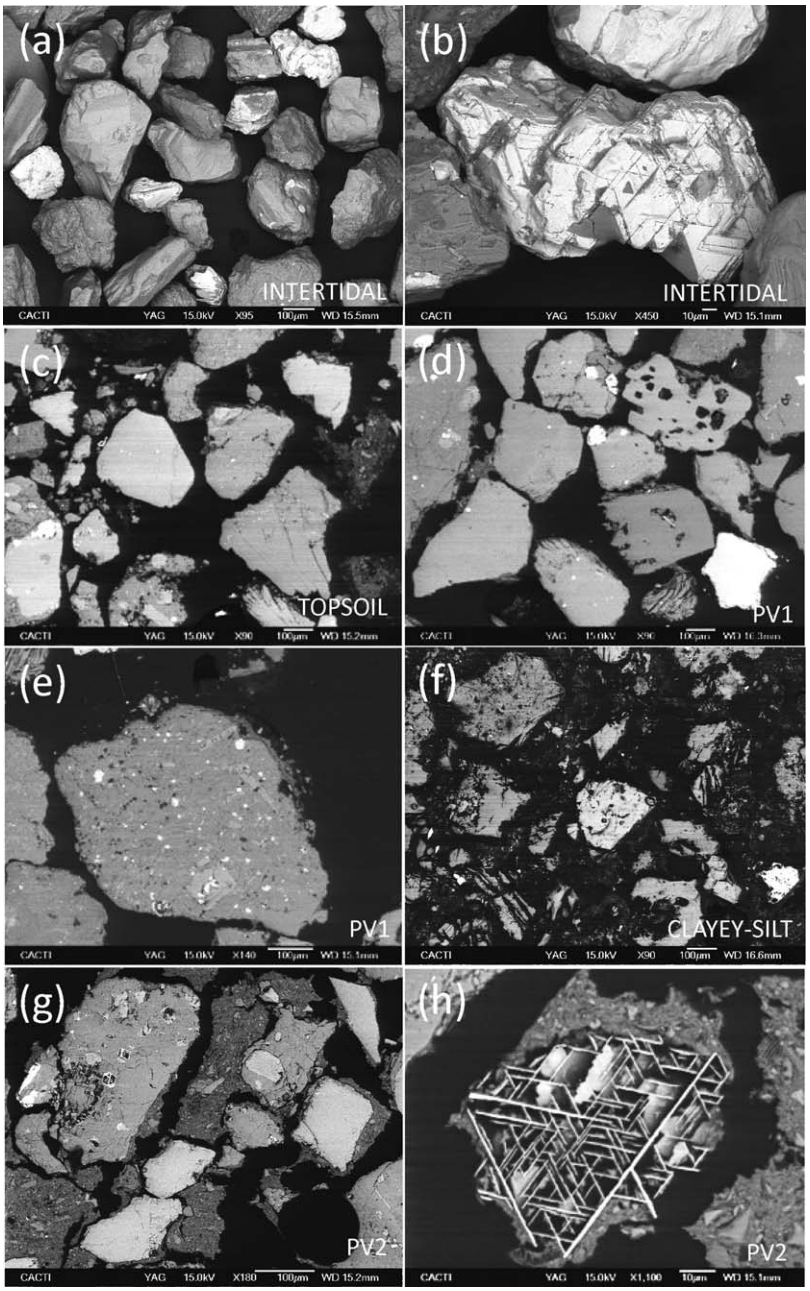

Figure 11. Scanning electron microscope images representative of the studied units. (a) Sand grains from the intertidal area of the present-day beach mounted on SEM stubs. (b) Fe-Ti iron oxide mineral showing the typical Ti-rich exolution lamellae (grey) in magnetite. The grain is mostly replaced by hematite. (c) Polished section of topsoil. These samples were very friable and the fine-grained matrix disaggregated and broke during preparation. However the original texture and composition of the matrix can be observed against the black background of the resin polymer used for consolidation. (d) PV1 unit showing the typical polymictic composition of the source area. (e) Fine-grained Fe-rich grains included in a volcanoclast. (f) Intense alteration of framework volcanic grains and associated occurrence of secondary montmorillonite-rich matrix in the clayey-silt unit. Fine-grained Fe-rich mineral are very apparent in the matrix. (g) PV2 unit showing similar textural and compositional characteristics as PV1. The primary matrix has been better preserved during preparation (circle). Some of the Fe-rich grains included in the large framework grain on the left have been altered (arrows). (h) Leucoxene showing the remaining Ti-rich exolution lamellae after alteration of titanomagnetites and/or ilmenite. See the unaltered beach sand grain in Figure 11b.

(χ_{fd} and χ_{fd}%) which are indicative of pedogenic magnetite exhibit in the clayey-silt unit the lowest values of the whole profile. The high coercivity component (component H) (Figures 7c–7f) has been identified as fine-grained (Ti)hematite with low Ti-content. Although this component has not been observed in thermomagnetic curves of the tsunamigenic units because of its low concentration (Figure 9), its presence in the

clayey-unit and PV2 is evident from IRM experiments (Figures 7 and 8). Since the (Ti)hematite contribution in PV2 is constant and slightly lower than in the clayey-silt unit and there are no changes in its coercivity values, we consider that this magnetic phase is not the result of a diagenetic process such as magnetite oxidation. Rather this fine-grained (Ti)hematite of igneous origin could be a product of high-temperature deuteric oxidation of (Ti)magnetite, constituting part of the detrital particles in this unit [*Dunlop and Ozdemir*, 1997].

The distinctive behavior between PV1 and PV2 might be associated with a different origin of these tsunamigenic units and/or different transportation processes of these magnetic minerals. Because not only the concentration but also the coercivity of the magnetic components are nearly constant in the PV1 unit, the sedimentation of PV1 and PV2 must have taken place under very different morphodynamic conditions. Differences in the wave energy and propagation direction, and in their transformation as they interact with the preexisting topography are sufficient to explain their distinct magnetic properties. Thus, the differences in the magnetic grain-size between PV2 (finer) and PV1 (coarser) could be related, not only to provenance but also to the specifics of the sediment dynamics during each event. This means that the event associated with the PV2 unit must have been different enough to facilitate the deposition of fine-grained magnetic particles. The coarser more porous sediment texture of PV2 may have favored the percolation of the very fine-grained magnetic grains through the unit. While the generally finer-grained and fining upward sequence observed in PV1 may have prevented such distribution of the very fine magnetic grains in the unit. If they were ever available for deposition during that event.

Most magnetic parameters exhibit a sharp change between PV1 and the underlying clayey-silt unit. *Ramírez-Herrera et al*. [2014] using a battery of multiproxy data (stratigraphic, particle size, geochemical, foraminifera, diatom, ostracods, and historical/ethnographic) identified a sharp erosional basal contact between PV1 and the clayey-silt unit. It was related to probably significant erosion produced by the large energy of the 22 June 1932 tsunami event. In addition, radiometric dating evidenced a marked hiatus of about 500 years between PV1 and the underlying unit. The magnetic results could also support this notable variation in detrital input in PV1 with respect the unit beneath suggested by *Ramírez-Herrera et al*. [2014], thus further validating the magnetic measurements as very useful proxies to improve the characterization of tsunamigenic units.

5.2. Provenance of the Tsunamigenic Deposits

Previous studies carried out in this sediment profile also identified some differences between the tsunamigenic units [*Ramírez-Herrera et al*., 2014]. The AMS study performed in these samples revealed differences between AMS fabrics along the profile, related to different stratigraphic units. Magnetic fabrics from the uppermost soil and the clayey-silt unit between PV1 and PV2 were construed as the result of a low-energy sedimentary environment. However, fabrics from PV1 show a preferential ESE–WNW orientation (116° azimuth) and those from PV2 a stronger E–W orientation (96° azimuth). Therefore, these units were interpreted as the result of currents flowing in those directions.

Petrology and particle size analysis performed by *Ramírez-Herrera et al*. [2014] on beach sand samples from the beach berm as well as from the intertidal beach area indicate that these sands are rich in volcanic rock fragments (mainly andesites). This fact has been also confirmed by the XRD and SEM analyses performed in this work (Figure 10). In addition, evidences of volcanic features were identified in the sediments during field sampling.

Taking into consideration previous results from *Ramírez-Herrera et al*. [2014] and the magnetic and mineralogical results obtained in this work, and trying to narrow down the source of the tsunamigenic sedimentary units we have also measured hysteresis and thermomagnetic curves of (1) pumice and ash samples from the last eruption of the Colima volcano (located 80 km NE from the Palo Verde trench) occurred before the 22 June 1932 tsunami event (1913 eruption) and (2) three lava flow samples from the Colima volcano (Ar-Ar ages ~34, 49, and 97 ka) (supporting information Figure S2). Thermomagnetic results, observed on ash samples clearly differ from those of PV1, indicating that the presence of windblown volcanic ashes from the last eruption of the Colima volcano before 1932 can be ruled out from being responsible for the enhancement of the magnetic contribution in the PV1 unit. On the other hand, although Ti-magnetite is the main magnetic phase in the three lava flow samples, additional information would be necessary to evaluate its potential influence in the tsunamigenic sedimentary deposits.

Carranza-Edwards et al. [2009] have shown that much of the differences in beach sand composition along the Cuyutlán barrier beach complex are due to the variability of source area rocks and local transport conditioned by wave climate, longshore currents, and local physiography. The mineralogical composition and texture of the local beach at the study site carried out in this work is consistent with *Carranza-Edwards et al*. [2009] results.

However, the compositional and textural differences observed between the PV1 and PV2 units and the interbedded clayey-silt unit needs the contribution of other mechanisms. The clayey-silt unit composition and texture can be explained by the action of intense postsedimentary edaphic processes. Montmorillonite results from alteration of volcanic lithic clasts and feldspar, increasing the quartz ratio relative to all the other constituents.

Differences in mineralogy between PV1 and PV2 are shown by the change in slope in the sand percentage versus SIRM diagram (Figure 3b). Furthermore, differences in PV1 and PV2 grain sizes (whole sediment texture) clearly indicate differences in energy between the two tsunamigenic events. Changes in the proportion of magnetic minerals in the sandy units (Figure 3b) indicate a change in provenance and/or in selective transport. Within PV1, and especially in PV2 both sand percentage and magnetic mineral concentration increase with depth. Upward grain-size fining sequences are a clear evidence of hydrodynamic sorting. This evidence provides a physical context in which magnetic grains sorting very likely occurs. The correlation between sand percentage and magnetic concentration (SIRM) is modulated by differences in hydraulic behavior controlled by the higher density of magnetic minerals and other minerals enriched in denser magnetic inclusions. These differences are particularly accentuated in the finest grain fraction where sedimentation is likely governed by Stoke's law. The hydraulic behavior of sand grains will be controlled by their size/density ratio under non-Stoke conditions (high turbulence), which results in background magnetic variability. Furthermore, the denser and smaller magnetic grains deposited at the last stage of the tsunamigenic flow may be sieved trough the coarse sand underneath, producing the magnetic grain fining downward trend showed by the ARM.

The complex patterns of vertical sorting observed in the magnetic mineral assemblages is also further explained by the complex structure of tsunami-related high-speed flows, as shown by *Jaffe et al*. [2012], where suspension graded beds are intermixed within massive or inversely graded intervals. Additionally, *Johnson et al*. [2016] have experimentally corroborated that differences in grain size at source or ponded water depths influence local entrainment, transport, and deposition conditions. Nevertheless, our previous interpretation does not necessary exclude the possibility of source-area related differences in the hydraulically sorted material. While overall differences in the magnetic composition between events may have been controlled at the source or during transport, smaller-scale within-unit variations are more likely hydraulically controlled during deposition.

There are several processes that can be equally invoked as potential mechanisms to explain different sources of the tsunamigenic deposits taking into account that there is no prior information about the paleostunami occurred around 1300 C.E. [*Ramírez-Herrera et al*., 2014]: (1) the manner in which tsunamis arrived at the shore and the backwash pattern; (2) a change in the coast morphology between the tsunami events associated with PV2 and PV1 that could influence the sediment origin and/or the hydrodynamic energy during sedimentation; (3) the energy of the paleotsunami event associated with the PV2 deposit was lower than that of the later event and the carrying capacity of the sediment-laden back-flow was not big enough as to rework the onshore deposits accumulated during runup flow. Indeed, *Ramírez-Herrera et al*. [2014] identified much more marine and marine-brackish taxa in PV2 than in PV1 samples.

6. Conclusions

Rock-magnetic analyses, XRD, and SEM experiments were conducted on samples from a trench located in the Palo Verde estuary (PV), near Cuyutlán, in the Colima coastal area, complementing the previous study carried out in this site by *Ramírez-Herrera et al*. [2014]. Although these authors identified two probable tsunamis related to tsunamigenic earthquakes of local origin (sand unit PV1 with the 22 June 1932 tsunami and sand unit PV2 with a probable paleotsunami that happened around 1300 C.E.), they also opened several questions regarding the provenance of deposits and the energy of both events.

The Palo Verde sedimentary sequence consists of five sedimentary units. Four of them have been magnetically characterized. Strong correlation between magnetic properties and the sedimentary stratigraphy has been observed. Ferrimagnetic minerals like Ti-magnetite control the magnetic signal and their concentration positively correlates to the sand content. Moreover, (Ti)hematite is also present in minor concentration mainly in the layers beneath the PV1 unit. Differences in both concentration and magnetic grain size of the magnetic phases have been detected between the two tsunamigenic units PV1 and PV2. Magnetic results such as the highest concentration of (Ti) magnetite in PV1 with respect to the lower units as well as the sharp contrast of the magnetic properties between this unit and the layer beneath could be related to the fact that the PV1 tsunamigenic deposit is the result of a very energetic event. Source-area differences (and/or in selective transport) between PV1 and PV2 deposits are supported by the change in the correlation pattern between sand percentage and magnetic concentration. On the other hand, hydrodynamic sorting could control the magnetic grain-size distribution in each tsunamigenic unit PV1 and PV2.

Detailed rock-magnetic and SEM techniques have proved to be an interesting complementary approach to characterize tsunami deposits. Therefore, they should be included together with other tools in a comprehensive study to help identify source areas and depositional process energy of tsunamigenic units.

Acknowledgments

M. F. Bógalo and M. Calvo-Rathert acknowledge financial support by projects BU0066U16 of the Junta de Castilla y León (Spain) and CGL2016–77560 from Ministerio de Economía y Competitividad (MINECO) both with European Regional Development Fund (ERDF) funding. M. T. Ramírez-Herrera acknowledges financial support by grants PAPPIT-UNAM-IN123609 and SEP-CONACYT-129456, and DGAPA-PASPA-2015. A. Goguitchaichvili acknowledges the partial financial support provided by DGAPA-PAPIIT IN101717 and CONACYT 252149. This work was also partially supported by Spanish projects CGL2015–66681-R and CGL2014–54117-REDT from MINECO and GRC2014/023 from Xunta de Galicia. K. J. Mohamed was funded by ED481C 2014/2 grant of the Xunta de Galicia. We are grateful to E. Font and an anonymous reviewer as well as to Associate Editor J. Feinberg for their useful and constructive comments and suggestions. The data used in this work are listed in the figures, tables, and references; any additional data can be made available upon request to the corresponding author (mfbogalo@ubu.es).

References

Atwater, B. F., and A. L. Moore (1992), A tsunami about 1000 years ago in Puget Sound, Washington, *Science*, *258*, 1614–1617.

Bloemendal, J., J. W. King, F. R. Hall, and S. J. Doh (1992), Rock magnetism of Late Neogene and Pleistocene deep-sea sediments: Relationship to sediment source, diagenetic processes and sediment lithology, *J. Geophys. Res.*, *97*, 4361–4375.

Bógalo, M. F., J. J. Villalaín, M. Calvo, M. I. González, A. I. Ortega, F. Heller, and A. Pérez-González (2014), New rock magnetic results from Galería cave in the Atapuerca palaeoanthropological site (northern Spain). Influence of solar irradiation in the edaphic generation of superparamagnetic grains?, paper presented at 14th Castle Meeting, New trends on Paleo, Rock and Environmental Magnetism, International Association of Geomagnetism and Aeronomy (IAGA) and Advanced Geoscience Instruments Company (AGICO), Evora, Portugal.

Bowles, J. A., M. J. Jackson, T. S. Berquó, P. A. Sølheid, and J. S. Gee (2013), Inferred time- and temperature-dependent cation ordering in natural titanomagnetites, *Nat. Commun.*, *4*, 1916, doi:10.1038/ncomms2938.

Carranza-Edwards, A., J. J. Kasper-Zubillaga, L. Rosales-Hoz, E. A. Morales-De La Garza, and R. Lozano-Santa Cruz (2009), Beach sand composition and provenance in a sector of the southwestern Mexican Pacific, *Rev. Mex. Cienc. Geol.*, *26*(2), 433–447.

Černý, J., M.-T. Ramírez-Herrera, M.-F. Bógalo, A. Goguitchaichvili, R. Castillo-Aja, J. Morales, J. A. Sanchez-Cabeza, A. C. Ruiz-Fernández, and A. C. Ruiz (2016), Magnetic record of extreme marine inundation events at Las Salinas site, Jalisco, Mexican Pacific coast, *Int. Geol. Rev.*, *58*, 342–357, doi:10.1080/00206814.2015.1075230.

Corona, N., and M. T. Ramírez-Herrera (2012), Mapping and historical reconstruction of the great Mexican 22 June 1932 tsunami, *Nat. Hazards Earth Syst. Sci.*, *12*(5), 1337–1352, doi:10.5194/nhess-12-1337-2012.

Corona, N., and M. T. Ramírez-Herrera (2015), Did an underwater landslide trigger the June 22, 1932 tsunami off the Pacific coast of Mexico?, *Pure Appl. Geophys.*, *172*, 3573–3587, doi:10.1007/s00024-015-1171-1.

Cumming, J. L. (1933), Los terremotos de junio de 1932 en los estados de Colima y Jalisco: Universidad de México, *31–32*, 68–104.

Cuven, S., R. Paris, S. Falvard, E. Miot-Noirault, M. Benbakkar, J.-L. Schneider, and I. Billy (2013), High-resolution analysis of a tsunami deposit: Case-study from the 1755 Lisbon tsunami in southwestern Spain, *Mar. Geol.*, *337*, 98–111, doi:10.1016/j.margeo.2013.02.002.

Dawson, A. G., and S. Shi (2000), Tsunami deposits, *Pure Appl. Geophys.*, *157*, 875–897.

Day, R., M. Fuller, and V.A. Schmidt (1977), Hysteresis properties of titanomagnetites: Grain-size and compositional dependence, *Phys. Earth. Planet. Inter. 13*, 260–267.[10.1016/0031–9201(77)90108-X]

Dearing, J. A., K. L. Hay, S. M. J. Baban, A. S. Huddleston, E. M. H. Wellington, and P. J. Loveland (1996), Magnetic susceptibility of soil: An evaluation of conflicting theories using a national data set, *Geophys. J. Int.*, *127*, 728–734.

Dearing, J. A., P. M. Bird, R. J. L. Dann, and S. F. Benjamin (1997), Secondary ferromagnetic minerals in Welsh soils: A comparison of mineral magnetic detection methods and implications for mineral formation, *Geophys. J. Int.*, *130*, 727–736.

Dunlop, D. J. (2002), Theory and application of the Day plot (M_{rs}/M_s versus Hcr/Hc): 1. Theoretical curves and tests using titanomagnetite data, *J. Geophys. Res.*, *107*(B3), 2056, doi:10.1029/2001JB000486.

Dunlop, D. J., and Ö. Ozdemir (1997), *Rock Magnetism, Fundamentals and Frontiers*, Cambridge Univ. Press, Cambridge, U. K.

Engel, M., and H. Brückner (2011), The identification of palaeo-tsunami deposits—A major challenge in coastal sedimentary research, *Coastline Rep.*, *17*, 65–80.

Evans, M. E., and F. Heller (2003), *Environmental Magnetism: Principles and Applications of Enviromagnetics*, Academic, San Diego, Calif.

Font, E., C. Nascimento, R. Omira, M. A. Baptista, and P. F. Silva (2010), Identification of tsunami-induced deposits using numerical modeling and rock magnetism techniques: A study case of the 1755 Lisbon tsunami in Algarve, Portugal, *Phys. Earth Planet. Inter*, *182*, 187–198, doi:10.1016/j.pepi.2010.08.007.

Font, E., C. Veiga-Pires, M. Pozo, S. Nave, S. Costas, F. Ruiz Muñoz, M. Abad, N. Simões, S. Duarte, and J. Rodríguez-Vidal (2013), Benchmarks and sediment source(s) of the 1755 Lisbon tsunami deposit at Boca do Rio Estuary, *Mar. Geol.*, *343*, 1–14, doi:10.1016/j.margeo.2013.06.008.

Forster, Th., M. E. Evans, and F. Heller (1994), The frequency dependence of low field susceptibility in loess sediments, *Geophys. J. Int.*, *118*, 636–642.

Goguitchaichvili, A., M. T. Ramírez-Herrera, M. Calvo-Rathert, B. Aguilar Reyes, Á. Carrancho, C. Caballero, F. Bautista, and J. Morales Contreras (2013), Magnetic fingerprint of tsunami-induced deposits in the Ixtapa-Zihuatanejo area, Western Mexico, *Int. Geol. Rev.*, *55*, 1462–1470, doi:10.1080/00206814.2013.779781.

Goto, K., K. Hashimoto, D. Sugawara, H. Yanagisawa, and T. Abe (2014), Spatial thickness variability of the 2011 Tohoku-oki tsunami deposits along the coastline of Sendai Bay, *Mar. Geol.*, *358*, 38–48, doi:10.1016/j.margeo.2013.12.015.

Goto, T., K. Satake, T. Sugai, T. Ishibe, T. Harada, and S. Murotani (2015), Historical tsunami and storm deposits during the last five centuries on the Sanriku coast, Japan, *Mar. Geol.*, *367*, 105–117, doi:10.1016/j.margeo.2015.05.009.

Grommé, C. S., T. L. Wright, and D. L. Peck (1969), Magnetic properties and oxidation of iron-titanium oxide minerals in Alae and Makaopuhi lava lakes, Hawaii, *J. Geophys. Res.*, *74*, 5277–5293.

Heslop, D., M. J. Dekkers, P. P. Kruiver, and I. H. M. van Oorschot (2002), Analysis of isothermal remanent magnetization acquisition curves using the expectation-maximization algorithm, *Geophys. J. Int.*, *148*, 58–64.

Hofmann, D. I., K. Fabian, F. Schmieder, B. Donner, and U. Bleil (2005), A stratigraphic network across the Subtropical Front in the central South Atlantic: Multi-parameter correlation of magnetic susceptibility, density, X-ray fluorescence and $\delta^{18}O$ records, *Earth Planet. Sci. Lett.*, *240*(3–4), 694–709.

Jaffe, B. E., K. Goto, D. Sugawara, B. M. Richmond, S. Fujino, and Y. Nishimura, (2012), Flow speed estimated by inverse modeling of sandy tsunami deposits: Results from the 11 March 2011 tsunami on the coastal plain near the Sendai Airport, Honshu, Japan, *Sediment. Geol.*, *282*, 90–109, doi:10.1016/j.sedgeo.2012.09.002.

Johnson, J. P. L., K. Delbecq, W. Kim, and D. Mohrig (2016), Experimental tsunami deposits: Linking hydrodynamics to sediment entrainment, advection lengths and downstream fining, *Geomorphology*, *253*, 478–490, doi:10.1016/j.geomorph.2015.11.004.

Kain, C., P. Wassmer, J. Goff, C. Chagué-Goff, C. Gomez, D. Hart, and D. Fierro (2016), Determining flow patterns and emplacement dynamics from tsunami deposits with no visible sedimentary structure, *Earth Surf. Processes Landforms*, *42*, 763–780, doi:10.1002/esp.4020.

Kain, C. L., C. Gomez, D. E. Hart, P. Wassmer, J. Goff, and C. Starheim (2014), Assessing topographic controls on flow direction in washover deposits using measurements of Magnetic Fabric, *Mar. Geol.*, *350*, 16–26, doi:10.1016/j.margeo.2014.01.010.

King, J., S. K. Banerjee, J. Marvin, and Ö. Özdemir (1982), A comparison of different magnetic methods for determining the relative grain size of magnetite in natural materials: Some results from lake sediments, *Earth Planet. Sci. Lett.*, *59*, 404–419.

Kortekaas, S., and A. G. Dawson (2007), Distinguishing tsunami and storm deposits: An example from Martinhal, SW Portugal, *Sediment. Geol.*, *200*, 208–221, doi:10.1016/j.sedgeo.2007.01.004.

Kruiver, P. P., M. J. Dekkers, and D. Heslop (2001), Quantification of magnetic coercivity components by the analysis of acquisition curves of isothermal remanent magnetization, *Earth Planet. Sci. Lett.*, *189*, 269–276, doi:10.1016/S0012-821X(01)00367-3.

Lancin, M., and A. Carranza (1976), Estudio geomorfológico de la bahía y la playa de Santiago en Manzanillo Colima, *Rev. Inst. Geol. UNAM*, *2*, 43–65.

Leonhardt, R. (2006), Analyzing rock magnetic measurements: The RockMagAnalyzer 1.0 software, *Comput. Geosci.*, *32*, 1420–1431, doi:10.1016/j.cageo.2006.01.006.

Liu, Q., A. P. Roberts, J. C. Larrasoaña, S. K. Banerjee, Y. Guyodo, L. Tauxe, and F. Oldfield (2012), Environmental magnetism: Principles and applications, *Rev. Geophys.*, *50*, RG4002, doi:10.1029/2012RG000393.

Lowrie, W. (1990), Identification of ferromagnetic minerals in a rock by coercivity and unblocking temperature properties, *Geophys. Res. Lett.*, *17*, 159–162.

Lyons, R., S. Tooth, and G. A. T. Duller (2014), Late Quaternary climatic changes revealed by luminescence dating, mineral magnetism and diffuse reflectance spectroscopy of river terrace paleosols: A new form of geoproxy data for the southern African interior, *Quat. Sci. Rev.*, *95*, 43–59.

Maher, B. (1986), Characterisation of soils by mineral magnetic measurements, *Phys. Earth Planet. Inter.*, *42*, 76–92, doi:10.1016/S0031-9201(86)80010-3.

Maher, B. A. (1998), Magnetic properties of modern soils and quaternary loessic paleosols: Paleoclimatic implications, *Palaeogeogr. Palaeoclimatol. Palaeoecol.*, *137*, 25–54, doi:10.1016/S0031-0182(97)00103-X.

Moore, A., G. Gelfenbaum, and R. Triyono (2006), Sedimentary deposits of the 26 December 2004 tsunami on the northwest coast of Aceh, Indonesia, *Earth Planets Space*, *58*, 253–258, doi:10.1186/BF03353385.

Morton, R. A., G. Gelfenbaum, and B. E. Jaffe (2007), Physical criteria for distinguishing sandy tsunami and storm deposits using modern examples, *Sediment. Geol.*, *200*, 184–207.

Okal, E. A., and J. C. Borrero (2011), The tsunami earthquake of 1932 June 22 in Manzanillo, México: Seismological study and tsunami simulations, *Geophys. J. Int.*, *187*(3), 1–17, doi:10.1111/j.1365-246X.2011.05199.x.

Özdemir, Ö., and D. J. Dunlop (2014), Hysteresis and coercivity of hematite, *J. Geophys. Res. Solid Earth*, *119*, 2582–2594, doi:10.1002/2013JB010739.

Peters, C., and M. J. Dekkers (2003), Selected room temperature magnetic parameters as a function of mineralogy, concentration and grain size, *Phys. Chem. Earth*, *28*, 659–667.

Ramírez-Herrera, M.-T., et al. (2014), Unearthing earthquakes and their tsunamis using multiple proxies: The 22 June 1932 event and a probable fourteenth-century predecessor on the Pacific coast of Mexico, *Int. Geol. Rev.*, *56*, 1584–1601, doi:10.1080/00206814.2014.951977.

Ramírez-Herrera, M. T., A. Cundy, V. Kostoglodov, A. Carranza-Edwards, E. Morales, and S. Metcalfe (2007), Sedimentary record of late Holocene relative sea-level change and tectonic deformation from the Guerrero Seismic Gap, Mexican Pacific coast, *Holocene*, *17*(8), 1211–1220, doi:10.1177/0959683607085127.

Ramírez-Herrera, M. T., et al. (2012), Extreme wave deposits on the Pacific coast of Mexico: Tsunamis or storms?—A multi-proxy approach, *Geomorphology*, *139–140*, 360–371, doi:10.1016/j.geomorph.2011.11.002.

Ramírez-Herrera, M. T., M. F. Bógalo, J. Černý, A. Goguitchaichvili, N. Corona, M. L. Machain, A. C. Edwards, and S. Sosa (2016), Historic and ancient tsunamis uncovered on the Jalisco-Colima Pacific coast, the Mexican subduction zone, *Geomorphology*, *259*, 90–104, doi:10.1016/j.geomorph.2016.02.011.

Reitz, A., C. Hensen, S. Kasten, J. A. Funk, and G. J. de Lange (2004), A combined geochemical and rock-magnetic investigation of a redox horizon at the last glacial/interglacial transition, *Phys. Chem. Earth*, *29*(13–14), 921–931.

Richmond, B. M., S. Watt, M. Buckley, B. E. Jaffe, G. Gelfenbaum, and R. A. Morton (2011), Recent storm and tsunami coarse-clast deposit characteristics, southeast Hawaii, *Mar. Geol.*, *283*, 79–89, doi:10.1016/j.margeo.2010.08.001.

Robertson, D. J., and D. E. France (1994), Discrimination of remanence-carrying minerals in mixtures, using isothermal remanent magnetisation acquisition curves, *Phys. Earth Planet. Inter.*, *82*, 223–234, doi:10.1016/0031-9201(94)90074-4.

Sánchez, A. J., and S. F. Farreras (1993), *Catálogo de tsunamis (maremotos) en la costa occidental de México*, Natl. Geophys. Data Cent., Boulder, Colo.

Schneider, J. L., C. Chagué-Goff, J. L. Bouchez, J. Goff, D. Sugawara, K. Goto, B. Jaffe, and B. Richmond (2014), Using magnetic fabric to reconstruct the dynamics of tsunami deposition on the Sendai Plain, Japan—The 2011 Tohoku-oki tsunami, *Mar. Geol.*, *358*, 89–106, doi:10.1016/j.margeo.2014.06.010.

Servicio Geológico Mexicano (2000), *Carta Geológico-Minera, Manzanillo E13–2-5, Colima y Jalisco*, México, México, D. F.

Shanmugam, G. (2012), Process-sedimentological challenges in distinguishing paleo-tsunami deposits, *Nat. Hazards*, *63*, 5–30, doi:10.1007/s11069-011-9766-z.

Singh, S. K., J. Havskov, and L. Astiz (1981), Seismic gaps and recurrence periods of large earthquakes along the Mexican subduction zone, *Bull. Seismol. Soc. Am.*, *71*, 827–843.

Singh, S. K., L. Ponce, and S. P. Nishenko (1985), The great Jalisco, Mexico, earthquakes of 1932: Subduction of the Rivera plate, *Bull. Seismol. Soc. Am.*, *75*(5), 1301–1313.

Spiske, M., J. Piepenbreier, C. Benavente, A. Kunz, H. Bahlburg, and J. Steffahn (2013), Historical tsunami deposits in Peru: Sedimentology, inverse modeling and optically stimulated luminescence dating, *Quat. Int.*, *305*, 31–44, doi:10.1016/j.quaint.2013.02.010.

Suarez, G., and P. Albini (2009), Evidence for Great Tsunamigenic Earthquakes (M 8.6) along the Mexican subduction zone, *Bull. Seismol. Soc. Am.*, *99*, 892–896, doi:10.1785/0120080201.

Sulpizio, R., E. Zanella, J. L. Macías, and R. Saucedo (2014), Deposit temperature of pyroclastic density currents emplaced during el Chichón 1982 and Colima 1913 eruptions, in *The Use of Palaeomagnetism and Rock Magnetism to Understand Volcanic Processes*, edited by M. H. Ort, M. Porreca, and J. W. Geissman, *Geol. Soc., London, Spec. Publ.*, 396, 35–49, doi:10.1144/SP396.5.

Torrent, J., Q.-S. Liu, J. Bloemendal, and V. Barron (2007), Magnetic enhancement and iron oxides in the Upper Luochuan Loess–Paleosol Sequence, Chinese Loess Plateau, *Soil Sci. Soc. Am. J.*, *71*, 1570–1578, doi:10.2136/sssaj2006.0328.

Veerasingam, S., R. Venkatachalapathy, N. Basavaiah, T. Ramkumar, S. Venkatramanan, and K. Deenadayalan (2014), Identification and characterization of tsunami deposits off southeast coast of India from 2004 Indian Ocean tsunami: Rock magnetic and geochemical approach, *J. Earth Syst. Sci.*, *123*(4), 905–921, doi:10.1007/s12040-014-0427-y.

Verma, S. P., and J. F. Luhr (1993), Sr-Nd-Pb isotope and trace element geochemistry of calc-alkaline andesites from Volcán Colima, Mexico, *Geofis. Int.*, *32*(4), 617–631.

Wassmer, P., and C. Gomez (2011), Development of the AMS method for unconsolidated sediments. Application to tsunami deposits, *Geomorpholie Relief Process.*, *3*, 279–290, doi:10.4000/geomorphologie.9491.

Wassmer, P., J.-L. Schneider, A. Fonfrege, F. Lavigne, R. Paris, and C. Gomez (2010), Use of Anisotropy of Magnetic Susceptibility (AMS) in the study of tsunami deposits: Application to the 2004 deposits on the eastern coast of Banda Aceh, North Sumatra, Indonesia, *Mar. Geol.*, *275*, 255–272, doi:10.1016/j.margeo.2010.06.007.

Wassmer, P. C., C. A. Gomez, T. Y. W. M. Iskandasyah, F. Lavigne, and J. Sartohadi (2015), Contribution of anisotropy of magnetic susceptibility (AMS) to reconstruct flooding characteristics of a 4220 BP tsunami from a thick unconsolidated structureless deposit (Banda Aceh, Sumatra), *Front. Earth Sci.*, *3*, 40, doi:10.3389/feart.2015.00040.